

## The effect of variable thermal diffusivity on kinematic models of subduction

P. Maierová,<sup>1,2</sup> T. Chust,<sup>1</sup> G. Steinle-Neumann,<sup>1</sup> O. Čadek,<sup>2</sup> and H. Čížková<sup>2</sup>

Received 21 December 2011; revised 23 May 2012; accepted 26 May 2012; published 11 July 2012.

[1] We examine the influence of variable thermal properties on the thermal state of a subducting slab in the upper mantle and the transition zone by combining a kinematic slab model with models of thermal conductivity. Thermal diffusivity and conductivity models for major mantle minerals in the MgO-SiO<sub>2</sub> system are developed based on experimental measurements on these minerals at high pressure and temperature. The models show significantly higher thermal conductivity for stishovite and clinopyroxene compared to the Mg<sub>2</sub>SiO<sub>4</sub> polymorphs and majorite garnet. In our subduction model we consider scenarios with a differentiated slab (basalt–harzburgite–pyrolite) in a pyrolite mantle and uniform composition for both the slab and the mantle (pyrolite or a pure Mg<sub>2</sub>SiO<sub>4</sub>-based system). The role of highly conductive pyroxene is examined by taking it into account in some models and replacing it in others with majorite garnet. This choice has a strong influence on the thermal state of the slab, shifting the depth of the –1000 K temperature anomaly by as much as 100 km. This is caused by faster cooling of the plate at the surface and thermal insulating effects once subducted. Temperature differences between models with variable thermal diffusivity and those with constant parameters can reach ~125 K, i.e. 10% of total thermal anomalies of the slab relative to an average geotherm. Taking into account the stable mineral phases we evaluate density variations between different models and find that variable thermal diffusivity results in a modest increase of negative buoyancy of the slab.

**Citation:** P. Maierová, T. Chust, G. Steinle-Neumann, O. Čadek, and H. Čížková (2012), The effect of variable thermal diffusivity on kinematic models of subduction, *J. Geophys. Res.*, 117, B07202, doi:10.1029/2011JB009119.

### 1. Introduction

[2] The subduction of lithosphere at convergent plate boundaries plays a crucial role in the process of mantle dynamics and cooling, and a detailed characterization of subduction is necessary for an understanding of Earth's heat engine. Studies based on the interpretation of seismic tomography suggest that subducting slabs penetrate the whole mantle and reach the core-mantle boundary within 120–250 Myr [e.g., Kývalová *et al.*, 1995; van der Meer *et al.*, 2010]. However, the fate of individual slabs may vary significantly [e.g., Bijwaard *et al.*, 1998; Fukao *et al.*, 2001] and the observed differences cannot be directly related to the basic characteristics of subduction, such as age and velocity of the lithospheric plate or dip of the subducting plate. It is obvious

that subduction is a strongly non-linear system and even small changes in parameters can influence its behavior.

[3] The factors determining the deformation of slabs in the mantle have been intensively studied by numerical modeling in conjunction with the results of mineral physics [e.g., Ita and King, 1998; Marton *et al.*, 1999; Nakagawa and Buffett, 2005; Ricard *et al.*, 2005]. Numerical models have looked at mechanical properties of mantle materials and their effects on the deformation of slabs in the upper mantle and transition zone [e.g., Schmeling *et al.*, 1999; van Hunen *et al.*, 2002, 2004; Běhounková and Čížková, 2008; Schmeling *et al.*, 2008; Billen, 2010], their descent into the lower mantle [e.g., Christensen, 1996; Čížková *et al.*, 2002; Enns *et al.*, 2005; Billen and Hirth, 2007; Běhounková and Čížková, 2008; Yoshioka and Naganoda, 2010] and the surface expression of the subduction process [e.g., Christensen, 1996; King, 2001; Tosi *et al.*, 2009; Krien and Fleitout, 2008; Faccenna *et al.*, 2009; Quinquis *et al.*, 2011]. Numerical studies have emphasized the importance of viscosity variations within the slab and in the ambient mantle [Čížková *et al.*, 2002; Stein *et al.*, 2004; Billen and Hirth, 2005; Quinteros *et al.*, 2010] and demonstrated effects associated with phase transitions [Jacobs and van den Berg, 2011; Bina and Kawakatsu, 2010; Marton *et al.*, 2005, 1999]. On the other hand, numerical models of subduction usually consider

<sup>1</sup>Bayerisches Geoinstitut, Universität Bayreuth, Bayreuth, Germany.

<sup>2</sup>Department of Geophysics, Faculty of Mathematics and Physics, Charles University, Prague, Czech Republic.

Corresponding author: P. Maierová, Department of Geophysics, Faculty of Mathematics and Physics, Charles University, V Holešovičkách 2, 180 00 Praha 8, Czech Republic. (maipe@karel.troja.mff.cuni.cz)

©2012. American Geophysical Union. All Rights Reserved.  
0148-0227/12/2011JB009119

**Table 1.** Simplified Mineralogical Model (mol. %) for the Different Lithologies Occurring in Subduction<sup>a</sup>

	Mg <sub>2</sub> SiO <sub>4</sub> ol/wa/ri	MgSiO <sub>3</sub> mj/cpx	SiO <sub>2</sub> st	MgSiO <sub>3</sub> pv	MgO pc
Pyrolite	60	40			
Harzburgite	80	20			
Basalt		92	8		
Lower mantle				83	17

<sup>a</sup>Abbreviations for the minerals are the following: olivine = ol, wadsleyite = wa, ringwoodite = ri, majorite garnet = mj, clinopyroxene = cpx, stishovite = st, perovskite = pv, and periclase = pc. The lower mantle is modeled uniformly for the slab and the ambient mantle as described in the text.

thermal diffusivity to be constant throughout the model domain. Notable exceptions are studies by *Marton et al.* [2005] and *Emmerson and McKenzie* [2007]. In *Marton et al.* [2005] a thermo-kinetic model of subduction is used to consider the influence of varying thermal conductivity for the Mg<sub>2</sub>SiO<sub>4</sub> polymorphs on temperature structure and the metastable olivine volume in the slab. *Emmerson and McKenzie* [2007] have looked at the thermal state of a slab with and without variable thermal parameters to assess their influence on seismicity in deeply subducting slabs.

[4] At this time thermal conductivity ( $k$ ) or diffusivity ( $D$ ) for the main upper mantle minerals has been estimated over a wide pressure ( $P$ ) and temperature ( $T$ ) range in experiments and from systematic considerations [*Xu et al.*, 2004; *Hofmeister*, 2008; *Hofmeister et al.*, 2007; *Hofmeister and Pertermann*, 2008; *Dobson et al.*, 2010; *Marquardt et al.*, 2009], although substantial uncertainty in the thermal transport properties remains. Variable  $k$  can be incorporated into models of subduction through the heat equation, and in the current paper we consider models of  $k$  for the different lithologies present in a slab in order to study their influence on its thermal structure and evolution.

[5] Subduction is modeled in a kinematic setup, for which we compute the corresponding temperature and density fields. The temperature fields are compared with a reference model relying on constant thermal diffusivity, and the influence of resulting temperature differences on density is discussed.

[6] The structure of the paper is as follows: In section 2 we define different lithologies in the subduction system, representing the basaltic oceanic crust, the depleted harzburgite component of the slab, and the ambient mantle in a simplified MgO-SiO<sub>2</sub> mantle. We then compile the available information on thermal diffusivity of the upper mantle minerals and compute the aggregate conductivity of the different phase assemblages. The model setup and the numerical approach used to simulate the evolution of temperature in a subducting slab are described in section 3. Section 4 presents results on the temperature field for different lithologies, different models of thermal conductivity, and setups for the subducting slab. In section 5 we discuss the influence of the lithological and temperature differences on the density distribution and whether such changes can potentially influence the style of subduction. The implications of the current study on our understanding of subduction are presented in section 6, in particular the possible influence of the

temperature variations on buoyancy and viscosity in a fully dynamic model.

## 2. Mineralogical Model

[7] The mineralogical model of the ambient mantle is based on pyrolite [*Palme and O'Neill*, 2003]. The two complementary lithological components of the slab, basalt and harzburgite, are created as a result of partial melting of pyrolite at mid-ocean ridges [*Baker and Beckett*, 1999]. Due to lack of a comprehensive and systematic data set on thermal conductivity or diffusivity for solid solutions in minerals both at ambient and high pressure we have restricted the compositional model to the MgO-SiO<sub>2</sub> system here, similar to early work on mantle thermodynamics and its influence on mantle properties and dynamics [*Ita and Stixrude*, 1992; *Ita and King*, 1994, 1998]. This simplification is also justified by large uncertainties in the available measurements of  $k$  and  $D$  for even the major mantle phases. In the MgO-SiO<sub>2</sub> model seven mineral phases occur in the upper mantle and the transition zone (Table 1): olivine (ol) and its high pressure polymorphs wadsleyite (wa) and ringwoodite (ri), clinopyroxene (cpx), majorite garnet (mj) and stishovite (st) that appears as a free phase in the SiO<sub>2</sub>-rich basalt (Table 1). In the MgSiO<sub>3</sub> system, which is particularly relevant for basalt, akimotoite is found stable at the base of the transition zone [*Ishii et al.*, 2011], but due to the lack of thermal diffusivity or conductivity measurements on this phase we had to replace akimotoite with mj.

[8] The lower mantle is part of the model domain, but effects of thermal conductivity on the state of the slab in the lower mantle are beyond the scope of the current study and it will not influence the thermal structure of the upper mantle and the transition zone. Consequently we do not distinguish between the lithology of the ambient mantle and the slab in the lower mantle. In the MgO-SiO<sub>2</sub> system the minerals that occur in the lower mantle (Table 1) are MgSiO<sub>3</sub> perovskite (pv) and periclase (pc) [*Ita and Stixrude*, 1992; *Piazzoni et al.*, 2007].

[9] We parameterize the thermodynamics of phase transitions in the mantle for the ol-wa, wa-ri and post-spinel transitions through their respective Clapeyron slopes [*Katsura and Ito*, 1989; *Akaogi et al.*, 1989; *Ohtani and Litasov*, 2006]. Kinetics and latent heat effects of the transitions in the Mg<sub>2</sub>SiO<sub>4</sub> system [*Akaogi et al.*, 1989; *Brearley et al.*, 1992; *Katsura et al.*, 2004] are not taken into account as these would mask the effects from variable thermal conductivity between different models considered. The dissolution of cpx into mj is modeled through a linear increase of the garnet content from 0% at 50 km to 100% at 500 km depth, following the actual dissolution trend of cpx in mj [*Xu et al.*, 2008; *Ricard et al.*, 2005].

[10] For the mineral phases listed in Table 1 we have compiled analytical relationships of thermal diffusivity  $D$  as a function of pressure and temperature (Table 2). Where the conversion between  $D$  and thermal conductivity  $k$  is needed, we use

$$D = \frac{k}{\rho c_p}, \quad (1)$$

**Table 2.** Thermal Diffusivity  $D$  Models for Minerals in the Upper Mantle and the Transition Zone<sup>a</sup>

	$D(T, P_{ref})$ ( $\text{mm}^2\text{s}^{-1}$ )	$\alpha_P$ ( $\text{GPa}^{-1}$ )	$P_{ref}$ (GPa)
Olivine	1.31 (298/T) <sup>0.68b</sup>	0.036	0 <sup>b</sup>
Wadsleyite	2.55 (298/T) <sup>0.72b</sup>	0.023	14 <sup>b</sup>
Ringwoodite	3.09 (298/T) <sup>0.79b</sup>	0.022	20 <sup>b</sup>
Majorite	0.62 (300/T) <sup>c</sup>	0.022	15 <sup>c,f</sup>
Stishovite	0.49 (690/T) <sup>d</sup>	0.09	0 <sup>g</sup>
Clinopyroxene	$1/(-0.138 + 0.00173T - 3.24 \cdot 10^{-7}T^2)^e$	0.04	0 <sup>f,h</sup>

<sup>a</sup>The functional dependence of  $D$  on  $P$  and  $T$  is discussed in the text.

<sup>b</sup>Xu *et al.* [2004].

<sup>c</sup>Dobson *et al.* [2010].

<sup>d</sup>Osako and Kobayashi [1979].

<sup>e</sup>Average from measurements for oriented Fe-bearing diopside on faces (100), (110) and (001) [Hofmeister and Pertermann, 2008].

<sup>f</sup>Osako *et al.* [2004].

<sup>g</sup>Yukutake and Shimada [1978].

<sup>h</sup>Hofmeister and Pertermann [2008].

with density  $\rho$  and isobaric heat capacity  $c_P$  computed at appropriate  $P$  and  $T$  with the thermodynamic database of Xu *et al.* [2008] as outlined below.

[11] Thermal diffusivity of the  $\text{Mg}_2\text{SiO}_4$  polymorphs (ol-wa-ri) has been studied experimentally up to 20 GPa and  $\sim 1400$  K by Xu *et al.* [2004], almost covering the range of pressures and temperatures relevant for the transition zone along a normal geotherm, i.e. up to 24 GPa and 1900 K.

[12] For pyroxenes, conductivity measurements on  $\text{MgSiO}_3$  enstatite are limited in temperature ( $<400$  K) and pressure ( $<6$  GPa) [Schloessin and Dvořák, 1972], in the stability range of ortho-enstatite [Kanzaki, 1991]. Clinopyroxenes have been studied over a wider temperature range at ambient pressure, with maximum temperatures of 1200–1600 K [Hofmeister and Pertermann, 2008]. The clinopyroxene most relevant for the mantle in that study was an Fe-bearing diopside. Thermal diffusivity measured for this diopside is consistent with that of ortho-enstatite from Schloessin and Dvořák [1972]. Pressure dependence of thermal conductivity in pyroxenes is poorly constrained, but measurements on jadeite [Osako *et al.*, 2004] provide values that are again consistent with the ortho-enstatite data of Schloessin and Dvořák [1972]. For the current work we combine the average of diffusivity on Fe-bearing diopside with different orientation from Hofmeister and Pertermann [2008] for  $T$ -dependence with  $P$ -dependence for jadeite from Osako *et al.* [2004].

[13] Diffusivity of majoritic garnet with a MORB-like composition has recently been determined by Dobson *et al.* [2010] at 15 GPa and temperatures of 400–1400 K. For the model of thermal diffusivity used here, measurements on pyrope garnet by Osako *et al.* [2004] have been combined with those by Dobson *et al.* [2010].

[14] For stishovite, measurements have been performed over a very limited pressure ( $<4$  GPa) [Yukutake and Shimada, 1978] and temperature ( $<550$  K) range [Osako and Kobayashi, 1979], similar to enstatite. Diffusivity data for st show a strong pressure dependence, and it has been suggested by Hofmeister *et al.* [2007] that this may be a consequence of the experimental setup; however, due to a lack of alternatives we use the data by Yukutake and Shimada [1978] and Osako and Kobayashi [1979]. It is worth noting that this has only a minor influence on the resulting

conductivity of the aggregate due to the low proportion of st present in the basaltic component of the slab (Table 1).

[15] Experimental data on thermal conductivity for lower mantle minerals at the relevant pressure and temperature conditions have been reported only very recently [Manthilake *et al.*, 2011], and here we rely on computational work by de Koker [2010] on the lower mantle phase aggregate, consisting of pv and pc.

[16] A radiative component to thermal conduction is observed at the temperatures in the upper mantle for transparent single crystals of the Mg-end-members or near-end-members of silicates considered here [Shankland *et al.*, 1979; Gibert *et al.*, 2005; Hofer and Schilling, 2002]. However, for the polycrystalline nature of the mantle with crystal sizes of 0.1–10 mm [Solomatov and Reese, 2008] and the presence of minor elements, most importantly Fe, the radiative component to thermal conduction is expected to be reduced although this is still under debate [Goncharov *et al.*, 2010; Hofmeister *et al.*, 2007; Thomas *et al.*, 2010; Keppeler and Smyth, 2005]. It is worth pointing out that the experiments used in the development of our diffusivity model do not capture the radiative component.

[17] For the minerals considered (Table 1) we treat the pressure and temperature dependence of thermal diffusivity with a separation of variables, i.e. fit  $P$ - and  $T$ -dependence independently at a reference temperature and pressure, respectively:

$$D(T, P) = D(T, P_{ref}) \cdot f(T_{ref}, P). \quad (2)$$

This is a widely used approach in dealing with thermal transport properties in laboratory and field measurements [Kukkonen *et al.*, 1999]. In equation (2) the temperature dependence is formulated as

$$D(T, P_{ref}) = \text{const} \cdot \left(\frac{T}{T_c}\right)^{-q}. \quad (3)$$

The temperature dependence varies significantly for the different minerals with  $q$  values between 0.68–1.0 (Table 2). For pyroxene (diopside) at low temperatures this does not provide a satisfactory fit as diffusivity values decrease much faster and we adopt a more complicated temperature-dependence, as given in Hofmeister and Pertermann [2008]. Diffusivity of stishovite is considerably higher than for the other minerals occurring in the different lithologies (Table 1). Due to a lack of a significant number of data points, a value of  $q = 1$  is used. Implicit in the formulation of equation (3) is a reference temperature:  $T_{ref}$  is determined as the temperature at which diffusivity is  $D(T, P_{ref}) = 1 \text{ mm}^2\text{s}^{-1}$ . This is not equal to the temperature constant  $T_c$  in equation (3).

[18] Pressure dependence is linearized with a coefficient  $\alpha_P$  around a reference pressure  $P_{ref}$  at  $T_{ref}$ , following the work on  $\text{Mg}_2\text{SiO}_4$  polymorphs by Xu *et al.* [2004]:

$$f(T_{ref}, P) = 1 + \alpha_P(P - P_{ref}). \quad (4)$$

Values for  $\alpha_P$  and the corresponding  $P_{ref}$  are given in the right column of Table 2. This approach differs from other work on the behavior of thermal diffusivity and conductivity with an exponential dependence on  $P$  [Hofmeister *et al.*, 2007; Dobson *et al.*, 2010]. However, for the current study

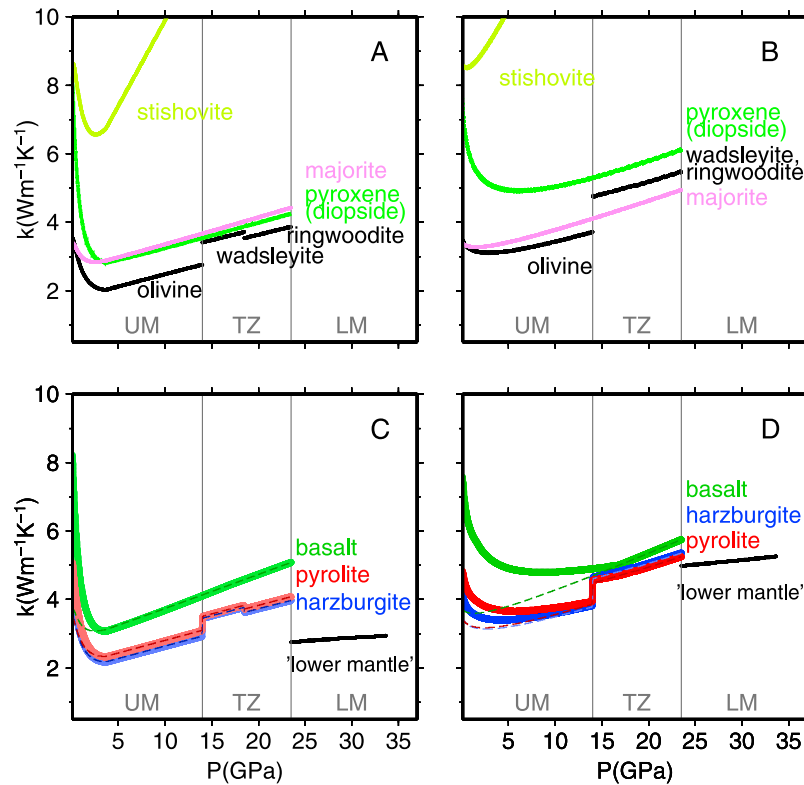


**Figure 1.** Thermal conductivity of (a, b) mineral phases and (c, d) phase assemblages along a mantle geotherm (Figures 1a and 1c) and slab geotherm (Figures 1b and 1d). Both geotherms are introduced in section 2 of the text. The dashed profiles in Figures 1c and 1d show the conductivity values for the phase aggregates when cpx is completely replaced by mj. The thin vertical lines separate the upper mantle (UM), transition zone (TZ) and lower mantle (LM).

we found the linear approach to be appropriate and robust for appropriate choices of  $P_{ref}$  (Table 2), especially when taking into account the large uncertainties in experiments.

[19] Thermal diffusivity for the different minerals determined here can be considered as upper bounds to  $D$  in solid solutions for all minerals and consequently for the phase assemblages of the different lithologies (Table 1). In a solid solution  $D$  decreases for compositions away from the respective end-member. This has been examined for various minerals, including garnets [Marquardt *et al.*, 2009] and the olivine solid solution [Pertermann and Hofmeister, 2006] at ambient conditions, and for pc and pv at high pressures [Manthilake *et al.*, 2011]. However, due to the restricted number of compositions studied and the large uncertainties on the measurements it is not possible to quantify the effect of other chemical components on thermal transport.

[20] For the subduction simulations thermal conductivity rather than diffusivity is used in the heat equation (see below), and  $D$  of the individual phases in the MgO-SiO<sub>2</sub> system is converted to  $k$  by means of density  $\rho$  and heat capacity  $c_P$  of these phases (Table 1) according to equation (1). The thermodynamic parameters  $\rho$  and  $c_P$  for the minerals in Table 1 are derived from their  $P - \rho - T$  equation-of-state according to the model by Stixrude and Lithgow-Bertelloni [2005a, 2005b] that combines a finite strain equation-of-state at room temperature with a Debye model for thermal excitations to obtain thermal pressure. The necessary model parameters are taken from the thermodynamic database of Xu *et al.* [2008].

Density  $\rho$  and heat capacity  $c_P$  for the phase assemblages are required for solving the heat equation.

[21] Thermal conductivity profiles of the different mineral phases along model mantle and slab geotherms are shown in Figure 1. The mantle geotherm is constructed by a half-space cooling model in the top 300 km, followed by an adiabat, as described in detail in section 3. The slab geotherm is taken according to Frohlich [2006]. As discussed above, conductivity values for stishovite are considerably larger than for other minerals along both temperature profiles. Similarly, at low pressure thermal conductivity of cpx is considerably larger than that of mj or ol. Differences in temperature dependence between the minerals become apparent when comparing values for the mantle (Figure 1a) and the slab geotherms (Figure 1b). For the lower temperatures in the slab, thermal conductivities are higher, with  $k$  for the Mg<sub>2</sub>SiO<sub>4</sub> polymorphs showing a modest increase. The increase of  $k$  for majorite with decreasing  $T$  is similar to that for the Mg<sub>2</sub>SiO<sub>4</sub> polymorphs, while both stishovite and pyroxene show a strong increase. It is worth noting that while for ambient mantle temperatures wa and ri show different values of  $k$ , for slab temperatures they become indistinguishable. Along the mantle geotherm conductivity of majorite is larger than that of the Mg<sub>2</sub>SiO<sub>4</sub> polymorphs; along the slab thermal profile  $k$  for mj is larger than for ol, but smaller than for wa or ri.

[22] Conductivity values of the aggregate lithologies (Table 1) – needed for the subduction simulations – are

**Table 3.** Mineralogical Models Used in This Study for the Kinematic Subduction

Model	Minerals Included	Lithologies for Slab	Remarks
<i>phb-px</i>	all	basalt, harzburgite and pyrolite	–
<i>phb-mj</i>	ol, wa, ri, mj, st	basalt, harzburgite and pyrolite	cpx replaced by mj
<i>p-px</i>	all	pyrolite	–
<i>p-mj</i>	ol, wa, ri, mj, st	pyrolite	cpx replaced by mj
<i>olwari</i>	ol, wa, ri	Mg <sub>2</sub> SiO <sub>4</sub>	–

computed as the average of the lower and upper Hashin-Shtrikman bounds [Hashin and Shtrikman, 1962]. Conductivity profiles for the mantle and slab geotherm are shown in Figures 1c and 1d, respectively. Profiles of  $k$  for pyrolite and harzburgite are similar, with the higher content of MgSiO<sub>3</sub> in pyrolite relative to harzburgite leading to slightly larger values of thermal conductivity in the upper mantle, where both mj and cpx have larger values of  $k$  than ol. In the transition zone, there is a difference in  $k$  between the two thermal profiles. As discussed above,  $k$  of mj is larger than  $k$  of wa and ri for the mantle geotherm, but smaller for the slab geotherm. As a consequence, the aggregate value for pyrolite is slightly larger than that of harzburgite for the mantle geotherm, and slightly lower for the slab geotherm.

[23] The lower mantle aggregate [de Koker, 2010] shows considerably smaller  $k$  than the transition zone for the thermal profile of the ambient mantle (Figure 1c), and a slightly lower value for the slab geotherm (Figure 1d).

[24] Basalt shows a considerably higher value of thermal conductivity, especially at low pressure. This is caused by the higher values for conductivity of st and cpx. With 92 mol. % content of cpx (Table 1) this mineral dominates basalt, and high values of thermal conductivity, especially at low pressures, yield considerably higher  $k$  for basalt compared to harzburgite and pyrolite (Figures 1c and 1d) up to ~15 GPa for the slab geotherm, and over the whole pressure range for the mantle geotherm. As other studies [Kobayashi, 1974] report much lower values of thermal conductivity of cpx than the ones used here from Hofmeister and Pertermann [2008], we consider two alternative scenarios for the thermal conductivity of the basalt: In addition to models that include thermal diffusivity of cpx for basalt (labeled *px*) we use thermal diffusivity profiles in which we replace cpx with mj for all lithologies (*mj*, dashed lines in Figures 1c and 1d). The latter case is also motivated by the fact that ultrabasic rocks show  $k \sim 4.5 \text{ Wm}^{-1}\text{K}^{-1}$  at ambient conditions [Zoth and Hänel, 1988], still considerably larger than the standard lithospheric value of thermal conductivity from Stein and Stein [1992], but in line with the values of conductivity used by Marton *et al.* [2005].

[25] In the current study, we are interested in the effect of variable thermal properties in a numerical model of subduction. We are aware that implementing the pressure-, temperature- and lithology-dependent thermal properties in a numerical model is rather difficult. Among others, the resolution of the thin basaltic (and harzburgitic) layer is particularly demanding, especially in a fully dynamic subduction model. For this reason we also explore model scenarios that are simplified (Table 3). Apart from models with a lithologically distinct slab (*phb*, which stands for pyrolite-harzburgite-basalt), we show models with pyrolitic composition in the whole simulation domain (*p*). We also test a

model where only olivine and its polymorphs are taken into account (*olwari*), which is the simplest reasonable model with  $P$ - and  $T$ -dependent thermal diffusivity in the upper mantle and the transition zone, similar to Marton *et al.* [2005].

### 3. Numerical Setup

[26] We use a kinematic model of subduction that is driven solely by the prescribed subduction velocity along the whole slab and neglects buoyancy forces associated with thermally induced density anomalies. We solve the continuity, momentum and heat equations:

$$\nabla \cdot \mathbf{v} = 0, \quad (5)$$

$$\nabla p - \nabla \cdot \boldsymbol{\sigma} = 0, \quad (6)$$

$$\rho c_p \frac{DT}{Dt} - \nabla \cdot k \nabla T = \boldsymbol{\sigma} : \dot{\boldsymbol{\epsilon}} - \alpha \rho v_z T g. \quad (7)$$

Symbols and parameters used in equations (5)–(7) are listed in Table 4. The thermodynamic parameters in the heat equation ( $\rho$ ,  $c_p$ ,  $\alpha$ ) are computed from the  $P$ - $\rho$ - $T$  equation of state in the mineral physics model, consistent with the model of  $k$  presented above. For the solution of the conservation equations (5)–(7) we use the finite element software Elmer ([www.csc.fi/english/pages/elmer](http://www.csc.fi/english/pages/elmer)).

[27] The rheological description combines linear diffusion creep (through the associated viscosity  $\eta_N$ ), power law dislocation creep ( $\eta_P$ ) and a power law stress limiter ( $\eta_L$ ) into a composite rheological model [e.g., van den Berg *et al.*, 1993]:

$$\boldsymbol{\sigma} = 2\eta_{eff} \dot{\boldsymbol{\epsilon}}. \quad (8)$$

Effective viscosity  $\eta_{eff}$  is calculated as follows [van Hunen *et al.*, 2004]:

$$\frac{1}{\eta_{eff}} = \frac{1}{\eta_N} + \frac{1}{\eta_P} + \frac{1}{\eta_L}. \quad (9)$$

The viscosities of the individual creep mechanisms are

$$\eta_N = A_N^{-1} \exp\left(\frac{E_N + PV_N}{RT}\right), \quad (10)$$

$$\eta_P = A_P^{-1/n} \dot{\boldsymbol{\epsilon}}^{(1-n)/n} \exp\left(\frac{E_P + PV_P}{nRT}\right), \quad (11)$$

$$\eta_L = \sigma_L \dot{\boldsymbol{\epsilon}}_L^{-1/n_L} \dot{\boldsymbol{\epsilon}}^{1/n_L-1}. \quad (12)$$

**Table 4.** Symbols and Parameters Used in the Current Manuscript

Parameter	Symbol	Value	Units
<i>Parameters for the Diffusivity Model</i>			
Temperature	$T$		K
Reference temperature	$T_{ref}$		K
Temperature constant	$T_c$		K
Hydrostatic pressure	$P$		Pa
Reference pressure	$P_{ref}$		Pa
Thermal diffusivity	$D$		$m^2 s^{-1}$
Thermal conductivity	$k$		$W m^{-1} K^{-1}$
Coefficient for temperature dependence of $D$	$q$		
Coefficient for pressure dependence of $D$	$\alpha_P$		$Pa^{-1}$
Density	$\rho$		$kg m^{-3}$
Specific heat	$c_p$		$J kg^{-1} K^{-1}$
<i>Parameters for the Kinematic Model</i>			
Velocity	$\mathbf{v}$		$ms^{-1}$
Pressure	$p$		Pa
Strain rate tensor	$\dot{\epsilon}$		$s^{-1}$
2nd invariant of the strain rate tensor	$\dot{\epsilon}$		$s^{-1}$
Deviatoric stress tensor	$\sigma$		Pa
Time	$t$		s
Thermal expansion coefficient	$\alpha$		$K^{-1}$
Gravitational acceleration	$g$	10	$ms^{-2}$
<i>Rheological Parameters</i>			
Effective viscosity	$\eta_{eff}$		Pa s
Viscosity — diffusion creep	$\eta_N$		Pa s
Viscosity — power law dislocation creep	$\eta_P$		Pa s
Viscosity — stress limiter	$\eta_L$		Pa s
Gas constant	$R$	8.3143	$JK^{-1} m^{-1}$
Viscosity stress exponent for $\eta_P$ <sup>a,b</sup>	$n$	3.5	
Yield stress	$\sigma_L$	$10^8$	Pa
Yield stress exponent	$n_L$	5	
Reference strain rate in yield strength determination	$\dot{\epsilon}_L$	$10^{-15}$	$s^{-1}$
<i>Upper Mantle and Transition Zone Parameters for <math>\eta_N</math> and <math>\eta_P</math><sup>a</sup></i>			
Pre-exponential parameter of diffusion creep	$A_N$	$1.92 \cdot 10^{-10}$	$Pa^{-1} s^{-1}$
Pre-exponential parameter of dislocation creep	$A_P$	$2.42 \cdot 10^{-15}$	$Pa^{-n} s^{-1}$
Activation energy of diffusion creep	$E_N$	300	$kJ mol^{-1}$
Activation energy of dislocation creep	$E_P$	540	$kJ mol^{-1}$
Activation volume of diffusion creep	$V_N$	$6 \cdot 10^{-6}$	$m^3 mol^{-1}$
Activation volume of dislocation creep	$V_P$	$15 \cdot 10^{-6}$	$m^3 mol^{-1}$
<i>Lower Mantle Parameters for <math>\eta_N</math> and <math>\eta_P</math><sup>b</sup></i>			
Pre-exponential parameter of diffusion creep	$A_N$	$6.63 \cdot 10^{-32}$	$Pa^{-1} s^{-1}$
Pre-exponential parameter of dislocation creep	$A_P$	$3.65 \cdot 10^{-15}$	$Pa^{-n} s^{-1}$
Activation energy of diffusion creep	$E_N$	208	$kJ mol^{-1}$
Activation energy of dislocation creep	$E_P$	285	$kJ mol^{-1}$
Activation volume of diffusion creep	$V_N$	$2.5 \cdot 10^{-6}$	$m^3 mol^{-1}$
Activation volume of dislocation creep	$V_P$	$1.37 \cdot 10^{-6}$	$m^3 mol^{-1}$

<sup>a</sup>Values based on Karato and Wu [1993].

<sup>b</sup>Values based on Yamazaki and Karato [2001], Frost and Ashby [1982], modified after Běhounková and Čížková [2008].

[28] In our kinematic model setup the geometry of the subducting plate is defined and does not change during the model calculation. A constant velocity is prescribed along the upper surface of the subducting plate, along the

subduction arc and the vertical portion of the subducting slab (Figure 2). Zero velocity is prescribed at the top of the overriding plate and free inflow/outflow at the sides and bottom boundaries. Our model domain is 1000 km deep and 2000 km wide. The initial condition for temperature is determined as follows: We calculate an adiabatic temperature profile for the entire model domain with a potential temperature of 1570 K at the surface. In constructing the adiabat we use the pressure and temperature dependent thermal expansivity for pyrolite from the mineral physics model, consistent with the use of thermodynamic parameters in the heat equation (7). The temperature in the uppermost 300 km is then evolved in time using the 1D heat equation (7) including only the conductive term with a prescribed constant surface temperature  $T = 273$  K and the adiabat temperature at a depth of 300 km. In most of our models we use a geotherm corresponding to a 100 Myr old plate. The conductive solution in the uppermost 300 km, followed by the adiabat in the lower part of the box, is also used as a boundary condition on both sides of the model domain. At the top boundary we prescribe a constant temperature  $T = 273$  K, at the bottom a heat flux corresponding to the adiabatic gradient.

[29] Both the subducting and overriding plates have a 10 km thick basaltic layer on top, followed by 40 km of harzburgite (green and blue lines in Figure 2). In order to resolve the thin basaltic layer, we use an unstructured grid of linear triangular elements with variable resolution. The resolution is about 3 km in the basaltic layer, 5 km in the harzburgitic layer of the slab and gradually decreases to 20 km in the ambient mantle far from the subducting and overriding plates. Between the subducting and overriding plates a narrow weak zone is introduced. Its low viscosity facilitates the decoupling of the subducting and overriding plates. The weak zone is 10 km wide and extends to a depth of 200 km. Its low viscosity is ensured by prescribing a yield stress  $\sigma_L = 10^6$  Pa, that is lower by two orders of magnitude than in the rest of the model domain (Table 4).

[30] In numerical models of slab deformation constant diffusivity is often considered throughout the mantle [e.g., Billen and Hirth, 2007; Čížková et al., 2007; Yoshioka and Naganoda, 2010]. As the main focus of the current paper is the study of variable pressure and temperature dependent

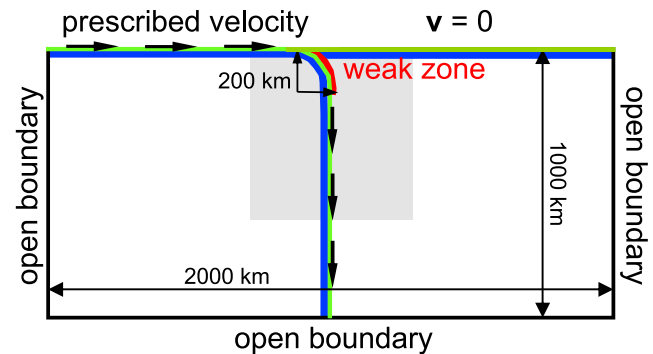


**Figure 2.** Setup of the model domain, boundary conditions for the momentum equation and lithologies (green = basalt, blue = harzburgite, white = ambient mantle, red = weak zone). The gray-shaded rectangle corresponds to the region shown in Figures 3–7.

thermal diffusion, we will discuss its effects on each case (Table 3) with respect to a reference model. In general, the choice of a representative reference model is rather difficult as the thermal parameters not only control the slab development with time, but also the initial temperature distribution. Therefore using a single reference model with constant parameters  $\rho$ ,  $c_p$ ,  $k$  and  $\alpha$  would produce high temperature differences relative to the models taking into account pressure, temperature and lithology dependent parameters just due to the very different initial condition. As a consequence, we define a reference model for each case (Table 3) separately: The model studied and the corresponding reference have the same initial geotherm calculated for variable thermal properties. During the time evolution, density  $\rho$  and heat capacity  $c_p$  are also the same in both models, but conductivity  $k$  is different: In the reference model, it is calculated such that  $D = 10^{-6} \text{m}^2 \text{s}^{-1}$  in equation (1) remains constant [Billen and Hirth, 2007].

[31] In the following we will use two quantities to demonstrate the effects of variable conductivity on temperature changes. First we introduce the temperature anomaly  $T_{anom}$  as the difference between the actual temperature distribution in a given model and the 1D depth dependent temperature following the mantle geotherm, calculated with the parameters of a given mineralogical model. The second quantity is the temperature difference  $T_{diff}$ , defined as the difference between the actual model temperature field and the temperature field in the corresponding reference model described above.

#### 4. Thermal Structure

[32] Conductivity and temperature fields are evaluated in the kinematic model as presented in the previous section. We consider a 100 Myr old plate subducting with a velocity of  $5 \text{ cm yr}^{-1}$ . Figures with results show a domain within the simulation box (2000 km width  $\times$  1000 km depth) of  $600 \text{ km} \times 660 \text{ km}$  (Figure 2), centered on the vertical portion of the subducted slab. Models are evaluated at the time when the slab tip would have reached the core-mantle boundary. In Figure 3, different rows show the different mineralogical models (Table 3), starting with the differentiated slabs (*phb*) in the upper two rows (*phb-px*, *phb-mj*). Uniform composition models are presented in the next two rows for pyrolite (*p-px* and *p-mj*) and the lowermost row shows the model *olwari*. The different columns show the conductivity field for the models (left), temperature anomaly with respect to the corresponding geotherm  $T_{anom}$  as discussed in section 3 (middle column), and temperature difference  $T_{diff}$  relative to a model with  $D = 10^{-6} \text{m}^2 \text{s}^{-1}$  constant (right column).

[33] The general conductivity distribution is similar for all models studied and will be described for *phb-px* as an example (Figure 3a). The subducting slab, as a cold region, has higher thermal conductivity than the surrounding mantle. This fact is illustrated in Figure 1 for analytical slab (Figures 1b and 1d) and mantle (Figures 1a and 1c) geotherms and it stems from the  $T^{-q}$  dependence of thermal diffusivity in equation (3). At  $\sim 200 \text{ km}$  depth, the conductivity of the surrounding mantle drops to less than  $2.5 \text{ Wm}^{-1} \text{K}^{-1}$  (red color in Figure 3a). This value corresponds to the minimum of conductivity for pyrolite in Figure 1c at  $\sim 4 \text{ GPa}$ , i.e. underneath the lithospheric part of the analytically computed geotherm.

In the transition zone, we observe an increase of  $k$  due to the ol-wa transition, while the wa-ri transition ( $\sim 550 \text{ km}$  depth) is almost invisible (Figures 1a and 1c).

[34] In detail, in the model *phb-px* (Figure 3a) the presence of cpx results in a highly conductive basaltic layer, visible in the narrow purple band in the shallow part of the slab which gradually changes to blue as cpx transforms to less conductive mj (Figure 1b). The conductivity of the basaltic layer is higher than  $7 \text{ Wm}^{-1} \text{K}^{-1}$  at shallow depths, i.e. significantly higher than that of ultrabasic rock at ambient conditions [Zoth and Hänel, 1988]. In the transition zone, pyroxene is mostly replaced by majorite and  $k$  is similar in the pyrolitic, basaltic and harzburgitic components of the slab, as already illustrated in Figure 1d. In the case where pyroxene is replaced by majorite (*phb-mj*), conductivity is reduced not only in the basaltic layer, but also in the rest of the slab and in the overriding plate (Figure 3d). The maximum value of conductivity in the upper 400 km of the model domain is then  $\sim 4 \text{ Wm}^{-1} \text{K}^{-1}$ .

[35] In the *p-px* model (Figure 3g), we replace the basaltic and harzburgitic layers of the slab by pyrolite, which is intermediate in conductivity between basalt and harzburgite (Figure 1d). As a consequence we do not observe any highly conductive band in the upper portion of the slab, but in shallow parts of the subducting and overriding plates  $k$  increases to more than  $5 \text{ Wm}^{-1} \text{K}^{-1}$  (blue wedge in Figure 3g). When the pyroxene component is replaced by majorite in the pyrolite model (*p-mj*, Figure 3j), conductivity in the upper mantle is lower than  $4 \text{ Wm}^{-1} \text{K}^{-1}$ , similar to *phb-mj* (Figure 3d). In both of these models (*phb-mj* and *p-mj*), the area characterized by relatively high conductivity (marked by green in the conductivity plot) is considerably narrower than in the corresponding models with pyroxene.

[36] In the model *olwari*, only  $\text{Mg}_2\text{SiO}_4$  polymorphs are considered and the conductivity follows the black lines in Figure 1a. In the upper mantle, the conductivity of olivine is lower than that of cpx or mj, which leads to conductivity values as low as  $\sim 2.0 - 2.3 \text{ Wm}^{-1} \text{K}^{-1}$  in the asthenosphere (dark red color in Figure 3m). In the transition zone, the ambient mantle conductivity of wa/ri is similar to that of mj and it is higher in the cold slab (Figures 1a and 1c). For this reason, conductivity in the transition zone in the *olwari* model (Figure 3m) is higher in the slab, but similar or slightly lower in the surrounding mantle than in the *p-mj* model (Figure 3j).

[37] The middle panels in Figure 3 show the temperature anomaly  $T_{anom}$  with respect to the mantle geotherm. Generally, it has a minimum of  $-1100 \text{ K}$  to  $-1150 \text{ K}$  in the shallow part of the bending slab and is lower by  $\sim 750 - 850 \text{ K}$  at the bottom of the transition zone. Further, the overriding plate is found to be colder by about  $300 \text{ K}$  at a depth of  $80 \text{ km}$ .

[38] If we compare the maximum depth of a temperature anomaly of  $-1000 \text{ K}$  in the different models, we can see that the slab is coldest in the *phb-px* model with a maximum depth of  $\sim 300 \text{ km}$  (Figure 3b), and warmest in the models without pyroxenes, i.e. *phb-mj* and *p-mj* with a maximum depth of  $\sim 200 \text{ km}$  (Figures 3e and 3k). This shows that higher conductivity of the slab (e.g. due to the basaltic layer in *phb-px*) implies a colder subducting slab, and we relate this effect to faster cooling of the plate at the surface prior to subduction. Surprisingly, the *olwari* model (Figure 3n) belongs to the intermediate models in this respect, although

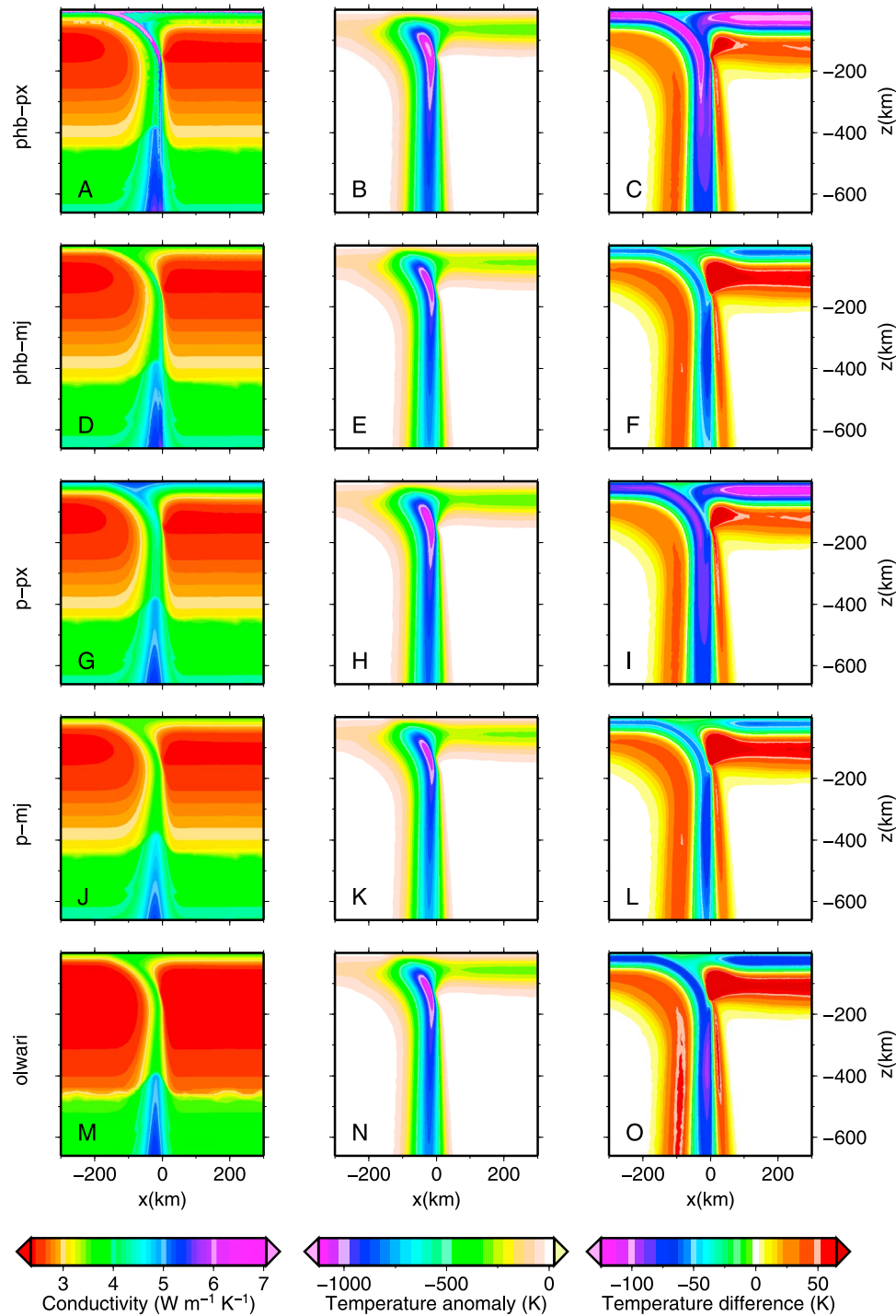


**Figure 3.** (left) Thermal conductivity  $k$ , (middle) temperature anomaly  $T_{anom}$  relative to the geotherm computed as described in section 3, and (right) temperature difference  $T_{diff}$  with respect to the corresponding reference model with constant diffusivity of  $10^{-6} \text{m}^2 \text{s}^{-1}$  for the five mineralogical/conductivity models considered (Table 3). In the kinematic slab model the subduction velocity is  $5 \text{cm yr}^{-1}$  and the age of the subducting plate is 100 Myr.

it has relatively low conductivity values for the slab and very low conductivity in the mantle. This is related to steep conductivity variations (Figure 3m) and demonstrates the effective thermal insulation of the cold slab due to the temperature dependence of  $k$ .

[39] The effect of variable thermal parameters is demonstrated in the right column of Figure 3 where the temperature difference  $T_{diff}$  with respect to the corresponding reference model with constant  $D = 10^{-6} \text{m}^2 \text{s}^{-1}$  is plotted. The subducting and overriding plates are significantly colder, while

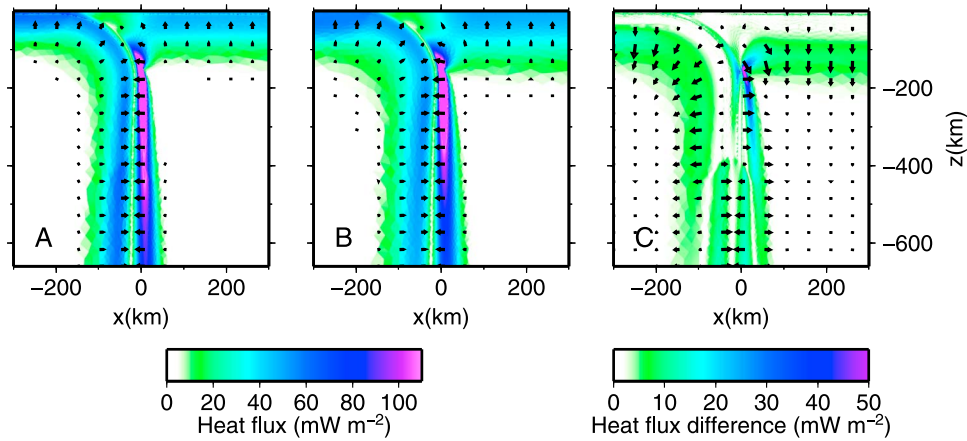


**Figure 4.** Heat flux  $-k\nabla T$  in the model *phb-px* with (a) variable thermal diffusivity and (b) constant diffusivity of  $10^{-6}\text{m}^2\text{s}^{-1}$ , and (c) their difference. Arrows show direction and relative magnitude of the heat flux (Figures 4a and 4b) and heat-flux difference (Figure 4c).

the asthenosphere and the areas along the slab are warmer than in the case of constant diffusivity. In the shallow part of the subducting slab, we observe the effect of faster cooling of the plate prior to subduction. Again, this effect is most prominent in the model *phb-px* (Figure 3c), where  $T_{diff}$  reaches values of  $-125\text{K}$  in the shallow parts of the subducting plate. Despite the high thermal conductivity of the slab  $T_{diff}$  remains high throughout the transition zone ( $-80\text{K}$ ), a somewhat counter-intuitive result that is examined in more detail below by considering the heat flow in the *phb-px* model with variable and constant thermal diffusivity (Figure 4). In the *phb-px* model, the asthenosphere below the subducting plate is warmer by  $\sim 30\text{K}$  and  $T_{diff}$  in and just above the mantle wedge reaches  $60\text{K}$  (Figure 3c).

[40] When the slab is not divided into basaltic and harzburgite layers, i.e. the whole model domain is pyrolitic (*p-px*, Figure 3i), the absence of the highly conductive basalt in the upper portion of the plates, combined with a somewhat lower conductivity of the slab in the transition zone (compare Figures 3a and 3g), yields a slab that is warmer than in model *phb-px* (Figure 3c). Still,  $T_{diff}$  within the slab remains as high as  $-80\text{K}$ . In the models without *px* (*phb-mj* and *p-mj*, Figures 3f and 3l, respectively),  $T_{diff}$  within the slab and overriding plate is smaller in magnitude: it reaches up to  $60\text{K}$  in the shallow part of the slab and  $\sim 50\text{K}$  at  $660\text{km}$  depth. As there are only small differences in conductivity between these two models (Figures 3d and 3j) it is not surprising that the resulting temperature and  $T_{diff}$  fields are similar as well.

[41] In the *owari* model (Figure 3o) we obtain more prominent temperature differences within the subducting slab (about  $-75\text{K}$  in the coldest portion of the slab all the way from the top to the transition zone) and around it (more than  $+50\text{K}$ ) compared to the *p-mj* model (Figure 3l).  $T_{diff}$  below the overriding plate exceeds  $60\text{K}$  and is the highest of all models examined, which can be related to the low conductivity of the asthenosphere.

[42] In all of the models considered, the internal parts of the plates are colder ( $T_{diff} < 0$ ) and the surrounding regions are warmer ( $T_{diff} > 0$ ) when variable diffusivity is taken into account. This is related to two effects: First, with higher

thermal conductivity the slab is colder when it enters the subducting arc as discussed above. Second, in models with variable thermal conductivity the slab is more effectively insulated from the ambient mantle, as is demonstrated in Figure 4 for the model *phb-px*. In Figures 4a and 4b we show the heat flux  $-k\nabla T$  in the case with variable and constant diffusivity, respectively. In both cases, the heat flux is highest in the outer part of the slab, where the temperature gradient is steepest. The arrows are pointing toward the center of the slab showing the direction of the heat flux. In the case with variable thermal properties (Figure 4a) the region with the heat flux higher than  $10^{-2}\text{Wm}^{-2}$  is visibly narrower and we observe higher heat flux in the slab below  $\sim 400\text{km}$  – due to an increase of thermal conductivity between the upper mantle and transition zone phase assemblage (Figure 1) – than in the constant diffusivity case (Figure 4b). The difference between the heat flux in the variable and constant diffusivity cases is plotted in Figure 4c. The difference is largest in the regions surrounding the cold slab, and the arrows pointing outwards from the slab show that the flux of heat into the slab is smaller when variable thermal properties are taken into account. In the transition zone this effect is reduced and in the slab even overcompensated (see arrows pointing toward the slab center in Figure 4c) by the high conductivity of this zone (Figure 3a).

[43] In addition to the effects of mineralogy, we examine the influence of plate velocity, plate age and slab dip on the thermal evolution of the model. In the previously discussed models, the plate was  $100\text{Myr}$  old, dipping vertically and subducting with a rate of  $5\text{cm yr}^{-1}$ . Figures 5a and 5b illustrate the effect of plate velocity: The  $100\text{Myr}$  old plate is now subducting with the plate velocity of  $10\text{cm yr}^{-1}$ . As one may expect, a faster subduction rate results in a colder slab. The temperature anomaly in the transition zone is higher by  $\sim 100\text{K}$  (Figure 5a) than in the slower slab (Figure 3b). The temperature difference with respect to the reference model (Figure 5b) is of a similar character as for the slower model (Figure 3c) except that  $T_{diff}$  in the shallow part of the subducting slab is now smaller by  $\sim 30\text{K}$  due to shorter cooling time at the surface. The effect of the slab dip on  $T_{diff}$  is demonstrated in Figure 5c, where the slab is subducting

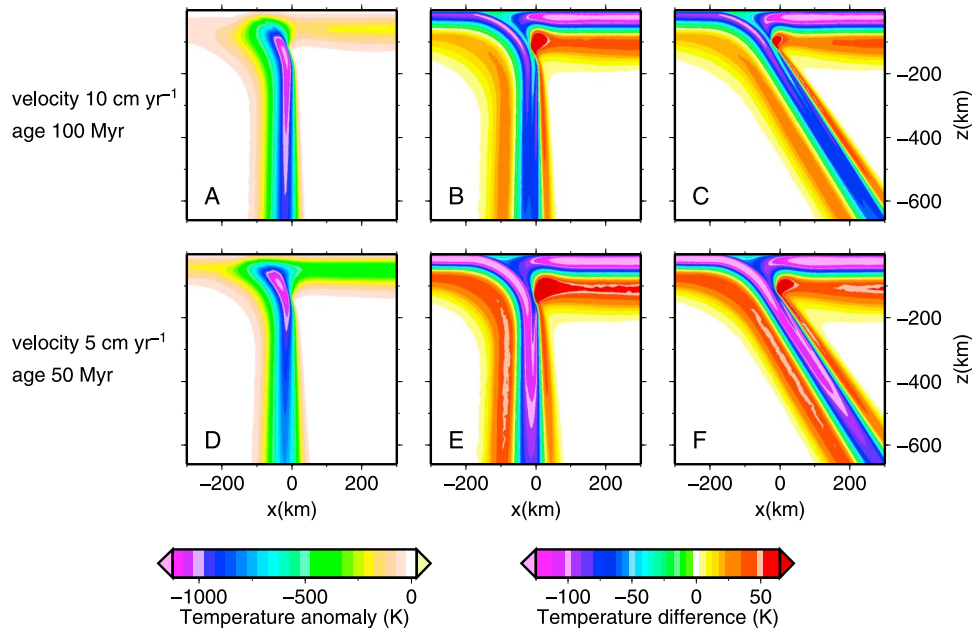


**Figure 5.** (left) Temperature anomaly  $T_{anom}$  and temperature difference  $T_{diff}$  for model *phb-px* with (middle) vertically subducting slab and (right) a slab dipping under the angle of 60 degrees. (a–c) The subduction velocity is  $10 \text{ cm yr}^{-1}$ , and the age of the subducting plate is 100 Myr. (d–f) Slab velocity is  $5 \text{ cm yr}^{-1}$ , and the subducting plate has an age of 50 Myr.

under an angle of 60 degrees. The comparison of the vertical (Figure 5b) and dipping slabs (Figure 5c) suggests that the effect of the slab dip is negligible in the kinematic setup.

[44] The fate of a younger and thus warmer and thinner plate is shown in the second row of Figure 5: The lithospheric age is 50 Myr, plate velocity is  $5 \text{ cm yr}^{-1}$ , and it subducts vertically (Figures 5d and 5e) or is dipping with an angle of 60 degrees (Figure 5f). When arriving at the transition zone, the younger plate is warmer by  $\sim 150 \text{ K}$  than the old one (cf. Figures 3b and 5d). Its temperature difference with respect to the reference model ( $T_{diff}$ ) with a constant diffusivity is much more prominent than for the older plate (cf. Figures 3c and 5e).

[45] Variations between individual models of the standard vertically subducting slab (Figure 3) are illustrated in Figure 6, where we show the difference between the temperature distributions for all pairs of models considered (Table 3). The different panels of Figure 6 show the temperature variations between the model noted above it and the model indicated to its left. For example, Figure 6a shows the temperature in the model *phb-px* relative to *olwari* (*phb-px* minus *olwari*). The temperature variations in the ambient mantle are negligible between some models (white areas around the slab), very small for other groups of models (yellow) and rather high between others (blue). These variations in the ambient mantle reflect the differences in the mantle geotherm – they are zero for the pairs with the same thermal expansivities, densities and heat capacities (Figures 6g and 6j), very small for pairs where thermal expansivities and heat capacities are similar, i.e. for pyrolite with and without cpx (Figures 6e, 6f, 6h, and 6i), and very high between the models with very different parameters, i.e. *olwari* vs. all other models (Figures 6a–6d).

[46] Slabs with cpx are colder than those in models without cpx, with negative variations of up to 125 K (Figures 6e and 6h). The models with pyroxenes also produce colder slabs than the *olwari* model (Figures 6a and 6b). On the other hand, the temperature variation inside the slab is very small (less than 25 K) between the models without cpx and the *olwari* model, indicated by the white and yellow areas in the shallow parts of the slabs in Figures 6c and 6d. The similar thermal structure stems from the fact that it is mainly controlled by thermal conductivity – and the conductivity for pyrolite without pyroxenes is rather close to that of olivine (Figure 1). By contrast, the deeper thermal structure in the ambient mantle, controlled by thermal expansivity and heat capacity, is very different in these models.

[47] Finally, we would like to point out the small difference between slabs that have a layered structure (*phb*) and pyrolite models (*p*), especially when pyroxenes are not included (Figure 6g).

## 5. Density Variations

[48] Together with the temperature fields, density has been extracted for the final state of all kinematic models. Figure 7 shows the results for two models that are representative for the differentiated (model *phb-px*, Figure 7a) and homogeneous slab (model *p-px*, Figure 7b), respectively. The sinking slab and its immediate surroundings are denser than ambient mantle in both models, and in analogy to the definition of  $T_{anom}$  we use the term density anomaly  $Q_{anom}$  for this density contrast. While the slab manifests itself as a coherent feature in the *phb-px* model through the basaltic layer (Figure 7a), it only appears as a diffuse high density region in the pyrolitic model *p-px* (Figure 7b). The basalt in *phb-px* has a marked density contrast to the pyrolite background due to its distinct

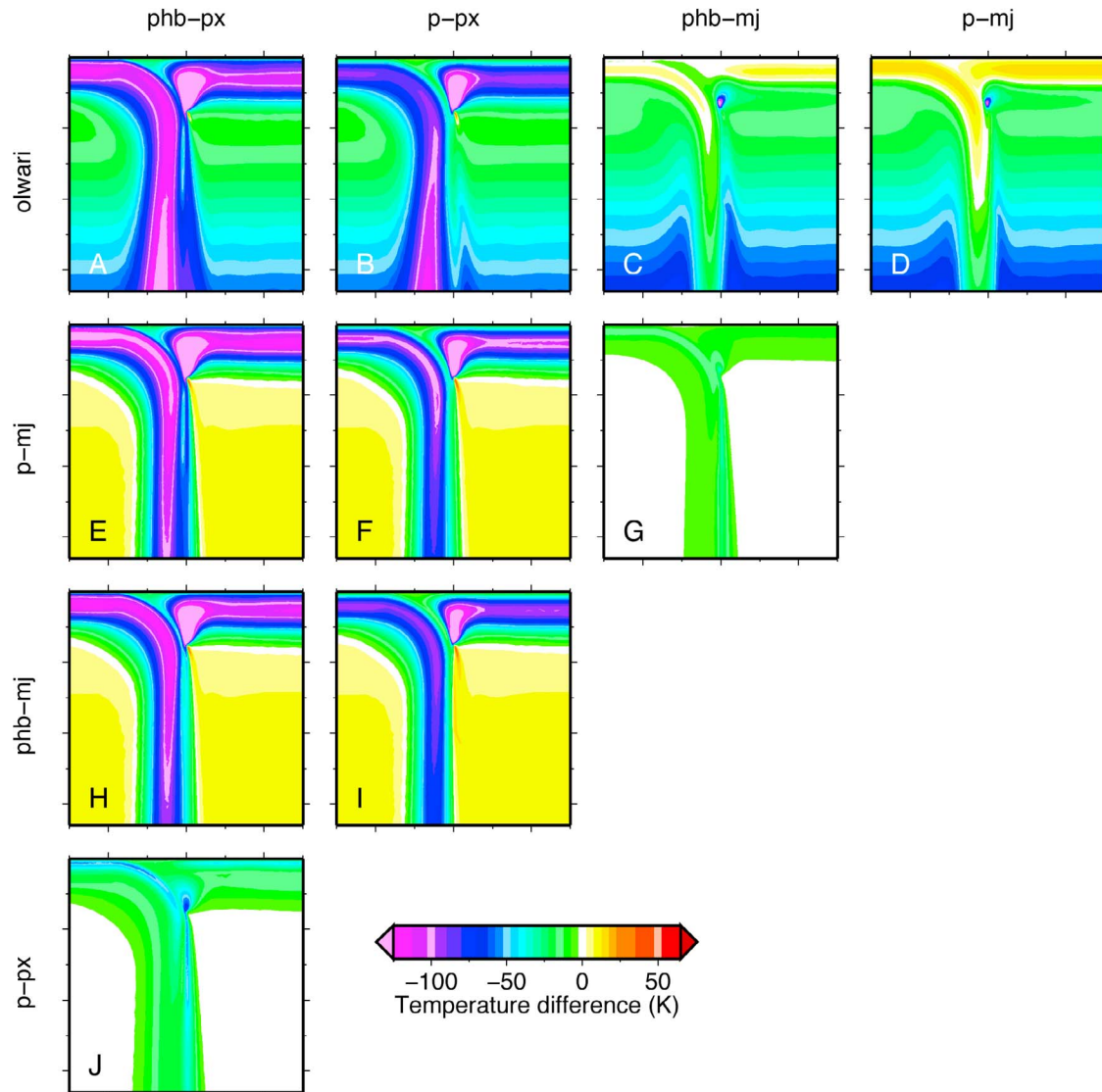


**Figure 6.** Differences between the temperature distributions for pairs of mineralogical models. The different panels show the temperature difference between the model indicated on top and the model indicated to the left (e.g. Figure 6a shows the temperature in the model *phb-px* minus the temperature in the model *olwari*). The x- and y-axis ranges are the same as for Figures 3–5.

bulk chemistry and different mineral phases (Table 1). For example, at 350 km depth the most abundant phases in the ambient mantle are ol and mj, with the density of the assemblage  $\sim 3.46 \text{ g cm}^{-3}$ . In the harzburgite layer of the slab the same phases are stable, but ol is more abundant, and the density of  $\sim 3.49 \text{ g cm}^{-3}$  is higher by 1%. The compositional change alone would lead to a lower density of 1%, but the lower temperature of the slab region overcompensates this effect. In the basaltic layer of the slab mj, cpx and st are stable, and the density of  $\sim 3.71 \text{ g cm}^{-3}$  is higher by  $\sim 7\%$  than that of the ambient mantle.

[49] At the boundary between the upper mantle and the transition zone the phase change from ol to wa also occurs at different depths in the ambient mantle and the harzburgite component of the slab due to different temperature, but even in the depth intervals where wa in the slab coexists with ol in the ambient mantle the density contrast between pyrolite and

basalt as well as between harzburgite and basalt is still larger than between harzburgite and pyrolite (Figure 7a). For the homogeneous model (*p-px*) the density increase of pyrolite in the slab region (Figure 7b), and hence  $Q_{anom}$ , is caused by lower temperatures to first order. As a consequence density contours are simply bent toward lower depths in the slab region.

[50] The behavior of the density field matches well with that found by Ricard *et al.* [2005] for more complex mineralogy but a similar model setup. In that study, the basaltic layer of the sinking differentiated slab is denser by  $\sim 6\%$  than the ambient mantle, while the density of the harzburgite layer is higher by  $\sim 1\%$ . In the case of homogeneous chemistry Ricard *et al.* [2005] show a broad density maximum around the slab region, similar to our results (Figure 7b): Large scale density structure correlates with the temperature field.

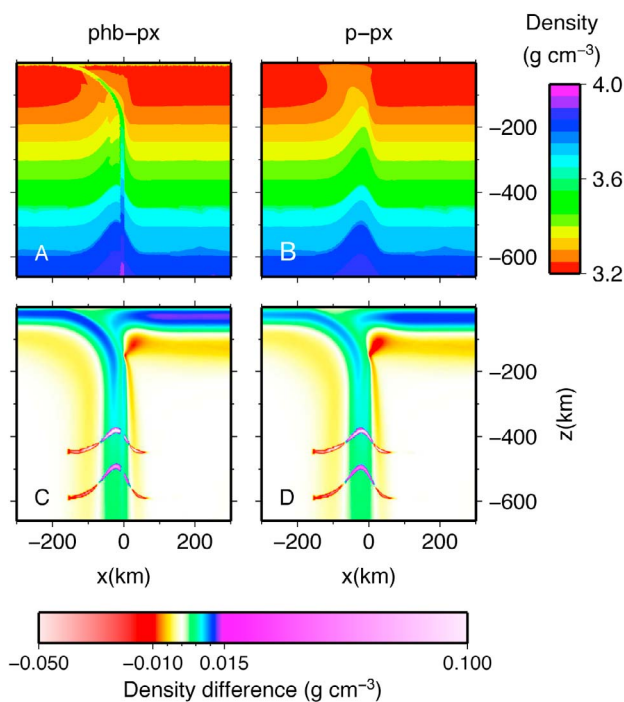


**Figure 7.** Density fields for the final thermal state of (a) a compositionally differentiated (*phb-px*) and (b) homogeneous (*p-px*) model and their difference  $Q_{diff}$  with respect to (c, d) the corresponding reference model with constant diffusivity of  $10^{-6} \text{m}^2 \text{s}^{-1}$ .

[51] Density differences ( $Q_{diff}$ ) caused by variable as opposed to constant diffusivity (Figures 7c and 7d) are focused in the regions of the phase transitions in the  $\text{Mg}_2\text{SiO}_4$  system, i.e. depth ranges of approximately 380–460 km and 490–600 km. The positive Clapeyron slope of the phase transitions ol-wa and wa-ri used in the current model [Akaogi *et al.*, 1989; Katsura and Ito, 1989] will lead to a shallower phase transition depth (7–10 km) at lower temperatures, and the resulting difference of mineralogy at the same depth between the constant and variable conductivity cases explains the larger  $Q_{diff}$ .

[52] Away from these regions  $Q_{diff}$  is about one order of magnitude smaller than  $Q_{anom}$ . The higher density of the slab region directly reflects the lower temperatures of these areas in the variable diffusivity models. For example, at 200 km depth in the harzburgite layer of the slab the density increases by  $\sim 0.01 \text{g cm}^{-3}$  for a drop of  $\sim 100 \text{K}$  ( $T_{diff}$ ) in temperature, which agrees with  $Q_{diff}$  in Figures 7c and 7d as well as  $T_{diff}$  in Figures 3c and 3i.

## 6. Conclusions

[53] Based on our kinematic simulations, we can conclude that the temperature differences between subduction models that take into account pressure-, temperature- and mineralogy-dependent thermal properties and those with constant thermal diffusivity are significant. In models with variable diffusivity, the interior of slabs is colder while their outer portion and the surrounding region is warmer. Depending on the mineralogical model and on the functional dependence

of thermal conductivity the temperature difference ( $T_{diff}$ ) can be as high as 125 K, i.e.  $\sim 10\%$  of the total temperature anomaly of the slab, with models containing highly conductive pyroxene showing the largest deviations. As a consequence the ol-wa and wa-ri phase transitions within the slab – with positive Clapeyron slope of both transitions – are moved to shallower depths (7–10 km) for the models with variable thermal diffusivity. The temperature difference of 125 K is significantly larger than the latent heat released at the ol-wa ( $\sim 60 \text{K}$ ) and wa-ri phase transitions ( $\sim 45 \text{K}$ ) [Katsura *et al.*, 2004] that would counteract the temperature differences from variable thermal diffusivity.

[54] The temperature differences among individual mineralogical/lithological models considered here are also quite significant and comparable to the overall effect of including variable diffusivity, reaching values in excess of 100 K. This is exemplified by the  $-1000 \text{K}$  temperature anomaly in the slab (difference to the ambient geotherm,  $T_{anom}$ ) being shifted downward from  $\sim 200 \text{km}$  to  $\sim 300 \text{km}$  for models containing pyroxene (*phb-px* and *p-px*). The downward shift of the isotherms observed here is less pronounced than in the model by Emmerson and McKenzie [2007]. At 400 km depth, i.e. near the upper mantle – transition zone boundary, the temperature anomaly still exceeds  $-900 \text{K}$ , with temperature differences relative to constant  $D$  models in the range of  $-90 \text{K}$ . This temperature difference could potentially lead to an extension of the olivine metastability region in the transition zone due to the kinetics of the ol-wa transition, beyond the thermodynamic stability limit of ol [Mosenfelder *et al.*, 2001; Marton *et al.*, 2005].

[55] Temperature variations on the order of 100 K account for one order of magnitude in viscosity and translate to  $\sim 10\%$  of buoyancy. Both effects would exert important effects on the evolution of a slab in a fully dynamic model. When including variable, realistic thermal properties, slabs should be more negatively buoyant and subduct faster. The resulting higher strain rate should affect the deformation of the slab through the non-linear stress-dependent rheology leading to dynamic feedback. Therefore, including proper mantle composition and related thermal properties may be crucial, especially for the numerical modeling of slab deformation in the upper mantle.

[56] On the other hand, our results show that dividing the slab into basalt and harzburgite layers has only a secondary effect on its thermal structure: The differences between temperatures obtained in a layered slab model (basalt, harzburgite, pyrolite) and a simple pyrolitic slab are small. This suggests that including the complex layered structure of the slab may not be necessary and a pyrolitic model is able to capture the most important features of shallow slab deformation. A similar conclusion can be drawn for the resulting density differences: Between a differentiated and a pyrolitic slab model, the density fields differ, as the denser basalt is missing in the latter. However, density averaged over the whole slab is nearly indistinguishable between these cases.

[57] Due to the kinematic setup the results presented here can provide only a rough estimate of possible effects of complex mineralogical models of thermal conductivity on subduction. Further modeling efforts, especially using fully dynamic models that take into account the non-linear

feedback mechanisms mentioned above will be necessary to better understand the role of thermal parameters on controlling slab dynamics.

[58] **Acknowledgments.** The work of P.M. at Bayerisches Geoinstitut has been made possible by the Marie Curie Research Training Network c2c (MRTN-CT-2006-035957). This research was also supported by grant SVV-2011-263308, the Czech Science Foundation grant P210/11/1366, the research project MSM0021620860 of the Czech Ministry of Education, and the German Research Foundation (DFG) with grant STE1105/6. We greatly appreciate helpful discussion with Nico de Koker, David Dobson, Simon Hunt, Tomoo Katsura, Ctirad Matyska, and David Yuen. Reviews by Craig Bina, an anonymous reviewer, and the Associate Editor David Sparks have improved the manuscript significantly.

## References

- Akaogi, M., E. Ito, and A. Navrotsky (1989), Olivine-modified spinel-spinel transitions in the system  $Mg_2SiO_4$ - $Fe_2SiO_4$ : Calorimetric measurements, thermochemical calculation, and geophysical application, *J. Geophys. Res.*, *94*, 15,671–15,685.
- Baker, M. B., and J. R. Beckett (1999), The origin of abyssal peridotites: A reinterpretation of constraints based on primary bulk compositions, *Earth Planet. Sci. Lett.*, *171*, 49–61.
- Běhounková, M., and H. Čížková (2008), Long-wavelength character of subducted slabs in the lower mantle, *Earth Planet. Sci. Lett.*, *275*, 43–53.
- Bijwaard, H., W. Spakman, and E. R. Engdahl (1998), Closing the gap between regional and global travel time tomography, *J. Geophys. Res.*, *103*, 30,055–30,078.
- Billen, M. I. (2010), Slab dynamics in the transition zone, *Phys. Earth Planet. Inter.*, *183*, 296–308.
- Billen, M. I., and G. Hirth (2005), Newtonian versus non-Newtonian upper mantle viscosity: Implications for subduction initiation, *Geophys. Res. Lett.*, *32*, L19304, doi:10.1029/2005GL023457.
- Billen, M. I., and G. Hirth (2007), Rheologic controls on slab dynamics, *Geochim. Geophys. Geosyst.*, *8*, Q08012, doi:10.1029/2007GC001597.
- Bina, C. R., and H. Kawakatsu (2010), Buoyancy, bending, and seismic visibility in deep slab stagnation, *Phys. Earth Planet. Inter.*, *183*, 330–340.
- Brearely, A. J., D. C. Rubie, and E. Ito (1992), Mechanisms of the transformation between the  $\alpha$ ,  $\beta$ , and  $\gamma$  polymorphs of  $Mg_2SiO_4$  at 15 GPa, *Phys. Chem. Miner.*, *18*, 343–358.
- Christensen, U. R. (1996), The influence of trench migration on slab penetration into the lower mantle, *Earth Planet. Sci. Lett.*, *140*, 27–39.
- Čížková, H., J. van Hunen, A. P. van den Berg, and N. J. Vlaar (2002), The influence of rheological weakening and yield stress on the interaction of slabs with the 670-km discontinuity, *Earth Planet. Sci. Lett.*, *199*, 447–457.
- Čížková, H., J. van Hunen, and A. P. van den Berg (2007), Stress distribution within subducting slabs and their deformation in the transition zone, *Phys. Earth Planet. Inter.*, *161*, 202–214.
- de Koker, N. (2010), Thermal conductivity of MgO periclase at high pressure: Implications for the D'' region, *Earth Planet. Sci. Lett.*, *292*, 392–398.
- Dobson, D. P., S. A. Hunt, R. McCormack, O. T. Lord, D. J. Weidner, L. Li, and A. M. Walker (2010), Thermal diffusivity of MORB-composition rocks to 15 GPa: Implications for triggering of deep seismicity, *High Pressure Res.*, *30*, 406–414.
- Emmerson, B., and D. McKenzie (2007), Thermal structure and seismicity of subducting lithosphere, *Phys. Earth Planet. Inter.*, *163*, 191–208.
- Enns, A., T. W. Becker, and H. Schmeling (2005), The dynamics of subduction and trench migration for viscosity stratification, *Geophys. J. Int.*, *160*, 761–775.
- Faccenna, C., E. Di Giuseppe, F. Funiciello, S. Lallemand, and J. van Hunen (2009), Control of seafloor aging on the migration of the Izu-Bonin-Mariana trench, *Earth Planet. Sci. Lett.*, *288*, 386–398.
- Frohlich, C. (2006), A simple analytical method to calculate the thermal parameter and temperature within subducted lithosphere, *Phys. Earth Planet. Inter.*, *155*, 281–285.
- Frost, H. J., and M. F. Ashby (1982), *Deformation Mechanism Maps*, Pergamon, Oxford, U. K.
- Fukao, Y., S. Widiyantoro, and M. Obayashi (2001), Stagnant slabs in the upper and lower mantle transition region, *Rev. Geophys.*, *39*, 291–323.
- Gibert, B., F. R. Schilling, K. Gratz, and A. Tommasi (2005), Thermal diffusivity of olivine single crystals and a dunite at high temperature: Evidence for heat transfer by radiation in the upper mantle, *Phys. Earth Planet. Inter.*, *151*, 129–141.
- Goncharov, A. F., V. V. Struzhkin, J. A. Montoya, S. Kharlamova, R. Kundargi, J. Siebert, J. Badro, D. Antonangeli, F. J. Ryerson, and W. Mao (2010), Effect of composition, structure, and spin state on the thermal conductivity of the Earth's lower mantle, *Phys. Earth Planet. Inter.*, *180*, 148–153.
- Hashin, Z., and S. Shtrikman (1962), A variational approach to the theory of the effective magnetic permeability of multiphase materials, *J. Appl. Phys.*, *33*, 3125–3131.
- Hofer, M., and F. R. Schilling (2002) Heat transfer in quartz, orthoclase, and sanidine at elevated temperature, *Phys. Chem. Miner.*, *29*, 571–584.
- Hofmeister, A. M. (2008), Pressure dependence of thermal transport properties, *Proc. Natl. Acad. Sci. U. S. A.*, *104*, 9192–9197.
- Hofmeister, A. M., and M. Pertermann (2008), Thermal diffusivity of clinopyroxenes at elevated temperature, *Eur. J. Mineral.*, *20*, 537–549.
- Hofmeister, A. M., M. Pertermann, and J. M. Branlund (2007), Thermal conductivity of the Earth, in *Treatise on Geophysics*, vol. 2, *Mineral Physics*, edited by G. Schubert, pp. 543–578, Elsevier, Amsterdam.
- Ishii, T., H. Kojitani, and M. Akaogi (2011), Post-spinel transitions in pyrolyte and  $Mg_2SiO_4$  and akimotoite-perovskite transition in  $MgSiO_3$ : Precise comparison by high-pressure high-temperature experiments with multi-sample cell technique, *Earth Planet. Sci. Lett.*, *309*, 185–197.
- Ita, J., and S. D. King (1994), Sensitivity of convection with an endothermic phase change to the form of governing equations, initial conditions, boundary conditions, and equation of state, *J. Geophys. Res.*, *99*, 15,919–15,938.
- Ita, J., and S. D. King (1998), The influence of thermodynamic formulation on simulations of subduction zone geometry and history, *Geophys. Res. Lett.*, *25*, 1463–1466.
- Ita, J., and L. Stixrude (1992), Petrology, elasticity, and composition of the mantle transition zone, *J. Geophys. Res.*, *97*, 6849–6866.
- Jacobs, M. H. G., and A. P. van den Berg (2011), Complex phase distribution and seismic velocity structure of the transition zone: Convection model predictions for a magnesium-endmember olivine-pyroxene mantle, *Phys. Earth Planet. Inter.*, *186*, 36–48.
- Kanzaki, M. (1991), Ortho clinoenstatite transition, *Phys. Chem. Miner.*, *17*, 726–730.
- Karato, S. I., and P. Wu (1993), Rheology of the upper mantle: A synthesis, *Science*, *260*, 83–108.
- Katsura, T., and E. Ito (1989), The system  $Mg_2SiO_4$ - $Fe_2SiO_4$  at high-pressures and temperatures: Precise determination of stabilities of olivine, modified spinel, and spinel, *J. Geophys. Res.*, *94*, 15,663–15,670.
- Katsura, T., et al. (2004), Olivine-wadsleyite transition in the system (Mg, Fe) $_2SiO_4$ , *J. Geophys. Res.*, *109*, B02209, doi:10.1029/2003JB002438.
- Keppler, H., and J. R. Smyth (2005), Optical and near infrared spectra of ringwoodite to 21.5 GPa: Implications for radiative heat transport in the mantle, *Am. Mineral.*, *90*, 1209–1212.
- King, S. (2001), Subduction zones: Observations and geodynamic models, *Phys. Earth Planet. Inter.*, *127*, 9–24.
- Kobayashi, Y. (1974), Anisotropy of thermal diffusivity in olivine, pyroxene and dunite, *J. Phys. Earth*, *22*, 359–373.
- Krien, Y., and L. Fleitout (2008), Gravity above subduction zones and forces controlling plate motions, *J. Geophys. Res.*, *113*, B09407, doi:10.1029/2007JB005270.
- Kukkonen, I. T., J. Jokinen, and U. Seipold (1999), Temperature and pressure dependencies of thermal transport properties of rocks: Implications for uncertainties in thermal lithosphere models and new laboratory measurements of high-grade rocks in the Central Fennoscandian shield, *Surv. Geophys.*, *20*, 33–59.
- Kývalová, H., O. Čadek, and D. A. Yuen (1995), Correlation analysis between subduction in the last 180 Myr and lateral seismic structure of the lower mantle: Geodynamical implications, *Geophys. Res. Lett.*, *22*, 1281–1284.
- Manthilake, G. M., N. Koker, D. J. Frost, and C. A. McCammon (2011), Lattice thermal conductivity of lower mantle minerals and heat flux from Earth's core, *Proc. Natl. Acad. Sci. U. S. A.*, *108*, 17,901–17,904.
- Marquardt, H., S. Ganschow, and F. R. Schilling (2009), Thermal diffusivity of natural and synthetic garnet solid solution series, *Phys. Chem. Miner.*, *36*, 107–118.
- Marton, F. C., C. R. Bina, S. Stein, and D. C. Rubie (1999), Effects of slab mineralogy on subduction rates, *Geophys. Res. Lett.*, *26*, 119–122.
- Marton, F. C., T. J. Shankland, D. C. Rubie, and Y. S. Xu (2005), Effects of variable thermal conductivity on the mineralogy of subducting slabs and implications for mechanisms of deep earthquakes, *Phys. Earth Planet. Inter.*, *149*, 53–64.
- Mosenfelder, J. L., F. C. Marton, C. R. Ross, L. Kerschhofer, and D. C. Rubie (2001), Experimental constraints on the depth of olivine metastability in subducting lithosphere, *Phys. Earth Planet. Inter.*, *127*, 165–180.
- Nakagawa, T., and B. A. Buffett (2005), Mass transport mechanism between the upper and lower mantle in numerical simulations of thermochemical mantle convection with multicomponent phase changes, *Earth Planet. Sci. Lett.*, *230*, 11–27.

- Ohtani, E., and K. D. Litasov (2006), The effect of water on mantle phase transitions, *Rev. Mineral. Geochem.*, **62**, 397–419.
- Osako, M., and Y. Kobayashi (1979), Thermal diffusivity of stishovite, *Phys. Earth Planet. Inter.*, **18**, P1–P4.
- Osako, M., E. Ito, and A. Yoneda (2004), Simultaneous measurements of thermal conductivity and thermal diffusivity for garnet and olivine under high pressure, *Phys. Earth Planet. Inter.*, **143**, 311–320.
- Palme, H., and H. St. C. O'Neill (2003), Cosmochemical estimates of mantle composition, in *Treatise on Geochemistry*, vol. 2, *The Mantle and Core*, edited by R. W. Carlson, pp. 1–38, Elsevier, Amsterdam.
- Pertermann, M., and A. M. Hofmeister (2006), Thermal diffusivity of olivine-group minerals at high temperature, *Am. Mineral.*, **91**, 1747–1760.
- Piazzoni, A. S., G. Steinle-Neumann, H.-P. Bunge, and D. Dolejš (2007), A mineralogical model for density and elasticity of the Earth's mantle, *Geochem. Geophys. Geosyst.*, **8**, Q11010, doi:10.1029/2007GC001697.
- Quinquis, M., S. Buitert, and S. Ellis (2011), The role of boundary conditions in numerical models of subduction zone dynamics, *Tectonophysics*, **497**, 57–70.
- Quinteros, J., S. V. Sobolev, and A. A. Popov (2010), Viscosity in transition zone and lower mantle: Implications for slab penetration, *Geophys. Res. Lett.*, **37**, L09307, doi:10.1029/2010GL043140.
- Ricard, Y., E. Mattern, and J. Matas (2005), Synthetic tomographic images of slabs from mineral physics, in *Earth's Deep Mantle: Structure, Composition, and Evolution*, *Geophys. Monogr. Ser.*, vol. 160, edited by R. D. van der Hilst et al., pp. 283–300, AGU, Washington, D. C.
- Schloessin, H. H., and Z. Dvořák (1972), Anisotropic lattice thermal conductivity in enstatite as a function of pressure and temperature, *Geophys. J. R. Astron. Soc.*, **27**, 499–516.
- Schmeling, H., R. Monz, and D. C. Rubie (1999), The influence of olivine metastability on the dynamics of subduction, *Earth Planet. Sci. Lett.*, **165**, 55–66.
- Schmeling, H., A. Babeyko, A. Enns, C. Faccenna, F. Funicello, T. Gerya, G. Golabek, S. Grigull, G. Morra, and J. van Hunen (2008), A benchmark comparison of subduction models, *Phys. Earth Planet. Inter.*, **171**, 198–223.
- Shankland, T. J., U. Nitsan, and A. G. Duba (1979), Optical-absorption and radiative heat-transport in olivine at high-temperature, *J. Geophys. Res.*, **84**, 1603–1610.
- Solomatov, V. S., and C. C. Reese (2008), Grain size variations in the Earth's mantle and the evolution of primordial chemical heterogeneities, *J. Geophys. Res.*, **113**, B07408, doi:10.1029/2007JB005319.
- Stein, C. A., and S. Stein (1992), A model for the global variation in oceanic depth and heat flow with lithospheric age, *Nature*, **359**, 123–129.
- Stein, C., J. Schmalzl, and U. Hansen (2004), The effect of rheological parameters on plate behaviour in a self-consistent model of mantle convection, *Phys. Earth Planet. Inter.*, **142**, 225–255.
- Stixrude, L., and C. Lithgow-Bertelloni (2005a), Thermodynamics of mantle minerals—I. Physical properties, *Geophys. J. Int.*, **162**, 610–632.
- Stixrude, L., and C. Lithgow-Bertelloni (2005b), Mineralogy and elasticity of the oceanic upper mantle: Origin of the low-velocity zone, *J. Geophys. Res.*, **110**, B03204, doi:10.1029/2004JB002965.
- Thomas, S., S. D. Jacobsen, C. R. Bina, A. F. Goncharov, D. J. Frost, and C. A. McCammon (2010), The effect of temperature and pressure on optical absorption spectra of transition zone minerals: Implications for the radiative conductivity of the Earth's interior, Abstract DI51C-1884 presented at 2010 Fall Meeting, AGU, San Francisco, Calif., 13–17 Dec.
- Tosi, N., O. Čadež, and Z. Martinec (2009), Subducted slabs and lateral viscosity variations: Effects on the long-wavelength geoid, *Geophys. J. Int.*, **179**, 813–826.
- van den Berg, A. P., P. E. van Keken, and D. A. Yuen (1993), The effects of a composite non-Newtonian and Newtonian rheology on mantle convection, *Geophys. J. Int.*, **115**, 62–78.
- van der Meer, D. G., W. Spakman, D. J. J. van Hinsbergen, M. L. Amaru, and T. Torsvik (2010), Towards absolute plate motions constrained by lower-mantle slab remnants, *Nat. Geosci.*, **3**, 36–40.
- van Hunen, J., A. P. van den Berg, and N. J. Vlaar (2002), On the role of subducting oceanic plateaus in the development of shallow flat subduction, *Tectonophysics*, **352**, 317–333.
- van Hunen, J., A. P. van den Berg, and N. J. Vlaar (2004), Various mechanisms to induce present-day shallow flat subduction and implications for the younger Earth: A numerical parameter study, *Phys. Earth Planet. Inter.*, **146**, 179–194.
- Xu, W., C. Lithgow-Bertelloni, L. Stixrude, and J. Ritsema (2008), The effect of bulk composition and temperature on mantle seismic structure, *Earth Planet. Sci. Lett.*, **275**, 70–79.
- Xu, Y., T. J. Shankland, S. Linhardt, D. C. Rubie, F. Langenhorst, and K. Klasinski (2004), Thermal diffusivity and conductivity of olivine, wadsleyite and ringwoodite to 20 GPa and 1373 K, *Phys. Earth Planet. Inter.*, **143–144**, 321–336.
- Yamazaki, D., and S. I. Karato (2001), Some mineral physics constraints on the rheology and geothermal structure of Earth's lower mantle, *Am. Mineral.*, **86**, 385–391.
- Yoshioka, S., and A. Naganoda (2010), Effects of trench migration on fall of stagnant slabs into the lower mantle, *Phys. Earth Planet. Inter.*, **183**, 321–329.
- Yukutake, H., and M. Shimada (1978), Thermal conductivity of NaCl, MgO, coesite and stishovite up to 40 kbar, *Phys. Earth Planet. Inter.*, **17**, 193–200.
- Zoth, G., and R. Hänel (1988), Appendix, in *Handbook of Terrestrial Heat-Flow Density Determination*, edited by R. Hänel, L. Rybach, and L. Stegena, pp. 449–466, Kluwer Acad., Dordrecht, Netherlands.